

Supplementary Information for Electron and Ion Transport in Semi-Dilute Conjugated Polyelectrolytes: View from a Coarse-Grained Tight Binding Model

David M. Friday and Nicholas E. Jackson*

*Department of Chemistry, University of Illinois at Urbana-Champaign, 505 S Mathews
Avenue, Urbana, Illinois, 61801, USA*

E-mail: jacksonn@illinois.edu

Contents

CPE Equilibration	1
Morphology Characterization	3
Bundling Algorithm	8
Network Structure Characterization	11
Electronic Structure Characterization	14
CPE Diffusion	19

CPE Equilibration

Correlation times for conjugated polyelectrolyte (CPE) structural properties are shown in Figure S1. Each decorrelation time is the result of a single trajectory and therefore some uncertainty is expected in the estimated values. Also, specific decorrelation metrics will exhibit different sensitivities to the specifics of the morphology, making the uncertainty variable as a function of concentration. The results show that the radius of gyration, end-to-end length, and fiber thickness of CPEs underwent at least one decorrelation time over the course of each simulation (150 $k\tau$ for poor solvent, 50 $k\tau$ for good solvent). The end-to-end vector (e.g. the rotation of the chains) did not decorrelate over the length of the simulations.

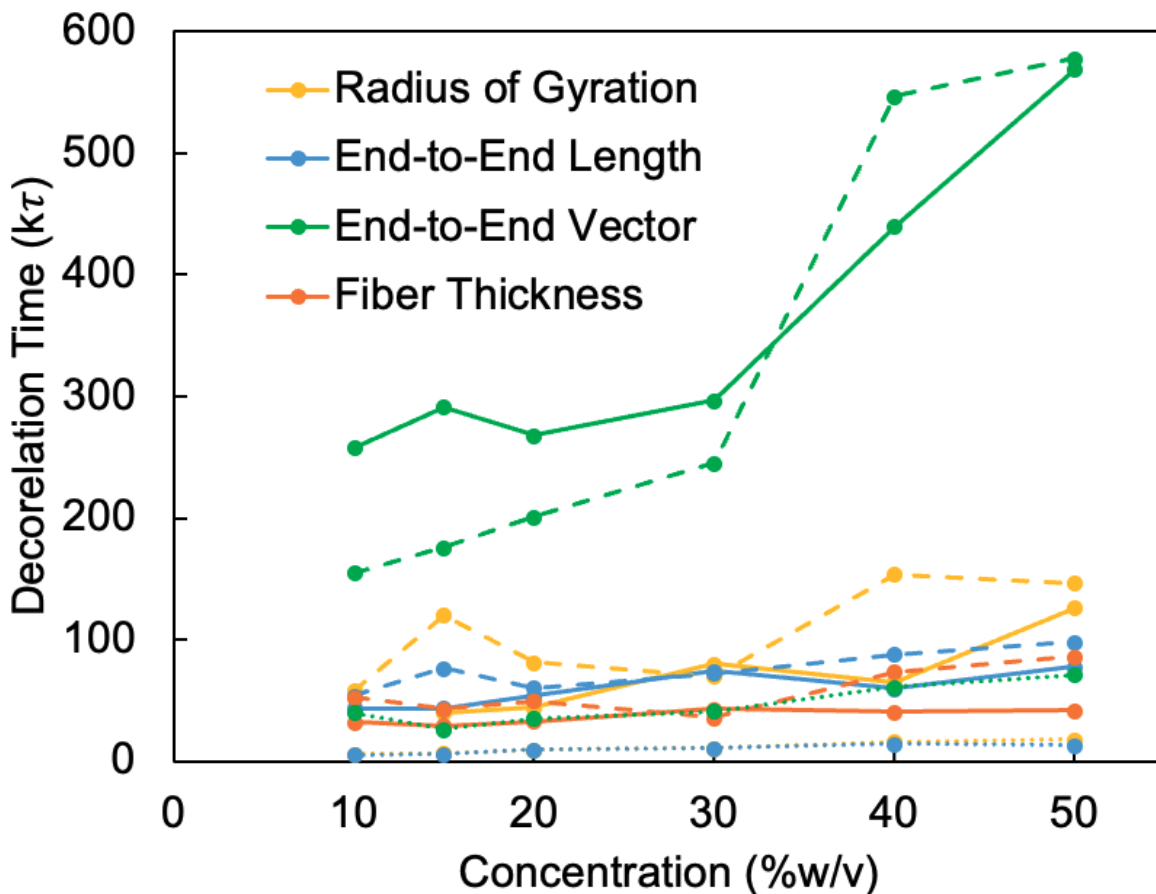


Figure S1: Decorrelation times of computed CPE properties during the production run ($50 k\tau$), after $100 k\tau$ of equilibration. The dotted lines correspond to good solvent; solid lines correspond to quenched poor solvent; and the dashed lines correspond to compressed poor solvent. The end-to-end vector metric is for a normalized vector, capturing the rotation of the polymer chains.

Morphology Characterization

CPE morphologies require characterizations on multiple length scales to understand how morphology impacts electronic mobility. Partial structure factor plots of the anisotropic backbone beads in Figure S2 show the expected scaling behavior of the position and height of the PE peak in good solvent, and the presence of a strong primary PE peak with a harmonic at higher q in poor solvent. The positions of the poor solvent peaks, as estimated

using the fit from Equation 12, are shown in Figure S3. Their scaling behavior is shown in Figure S4 and S6, showing a transition from sub-0.5 scaling, to 0.2 scaling in the quenched morphologies, and ~ 0.3 scaling in the compressed morphologies. The π -stacking distance in the structure factors was expected to be at $\sim 1\sigma$, however monomers in π -stacked chains were often offset from each other, increasing the average center-to-center distance between anisotropic beads in simulations to approximately $\sim 1.1\sigma$.

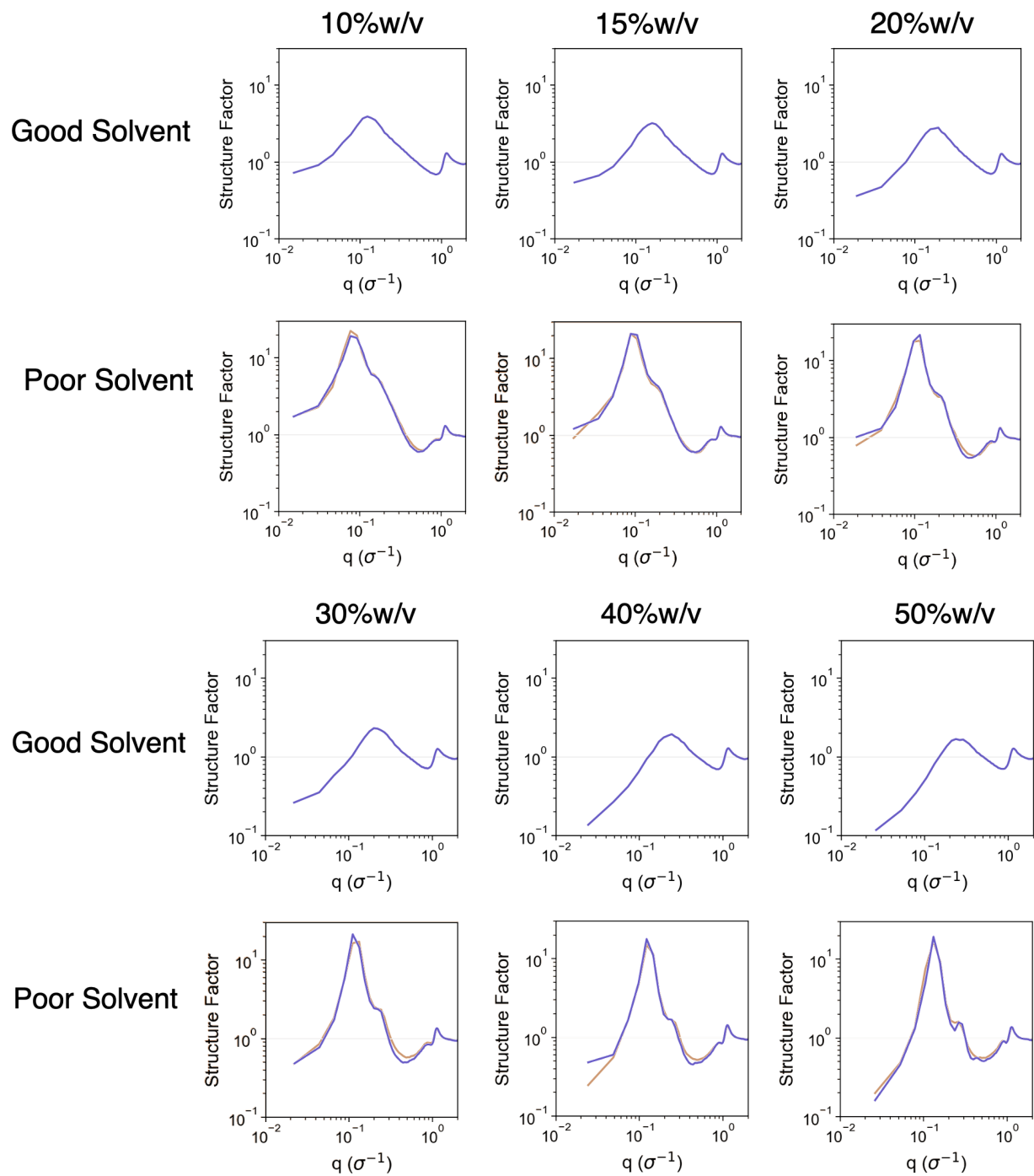


Figure S2: Structure factor of the good solvent and poor solvent morphologies vs. concentration. The poor solvent plots contain both the compressed (purple) and quenched (orange) results, overlaid. All q -values are divided by 2π to aid interpretation, and $1 \sigma \sim 0.5 \text{ nm}$ in real units.

Quenched	10 w/v	15 w/v	20 w/v	30 w/v	40 w/v	50 w/v
A	0.60	0.79	0.88	1.31	1.33	1.56
n	-0.50	-0.68	-0.83	-1.33	-1.33	-1.46
B	17	18	17	17	14	16
q1	0.08	0.10	0.11	0.12	0.13	0.13
L1	48	43	40	40	36	36
m	3.1	3.1	3.0	3.0	3.2	3.5
C	5.1	3.9	3.0	2.1	1.4	1.4
q2	0.15	0.18	0.19	0.22	0.24	0.25
L2	13	14	15	15	17	17
q2/q1	1.75	1.82	1.83	1.84	1.86	1.88

Concentrated	10 w/v	15 w/v	20 w/v	30 w/v	40 w/v	50 w/v
A	0.47	0.59	3.10	1.85	3.46	1.56
n	-0.49	-0.69	-3.00	-2.03	-3.00	-1.54
B	16	19	19	20	18	17
q1	0.08	0.10	0.11	0.12	0.13	0.14
L1	46	47	46	46	48	41
m	3.5	2.6	3.1	2.9	2.6	3.1
C	5.4	3.7	3.6	2.2	1.4	1.4
q2	0.14	0.18	0.18	0.21	0.23	0.27
L2	12	15	13	16	14	22
q2/q1	1.70	1.82	1.69	1.80	1.81	1.95

Figure S3: Structure factor fit parameters for each poor solvent CPE simulation. Parameters are from Equation 12 (see main text)

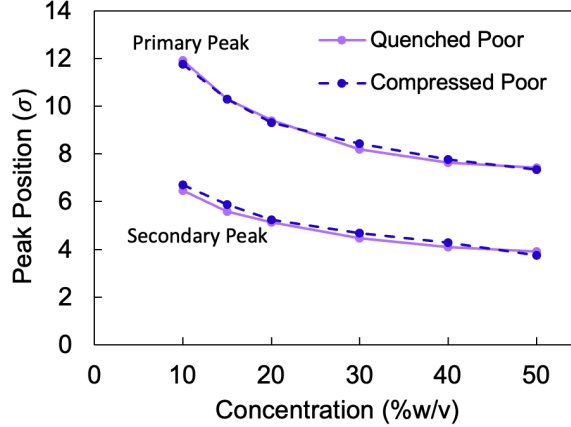


Figure S4: Positions of the primary and secondary PE peaks vs. concentration. Solid and dashes lines correspond to quenched and compressed morphologies, respectively.

Figure S5 shows the structure factor for all beads in the CPE chain (backbone, sidechain, and pendant ion beads), showing the loss of intensity in the secondary harmonic PE peak when the full chain is present (compare to Figure 3 in main text). However, the position of the secondary harmonic appears to be unchanged.

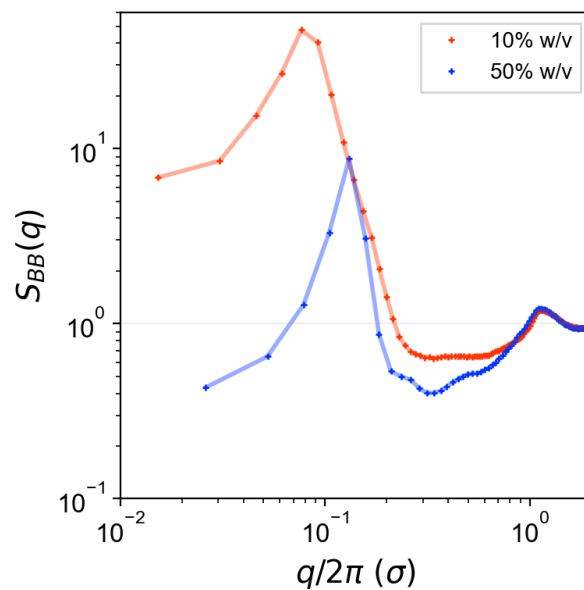


Figure S5: Structure factor for the entire polymer (backbone, sidechain, and pendant cation beads) for the compressed simulations showing the loss of intensity from the secondary CPE peak. Lines connecting points are guides for the eye.

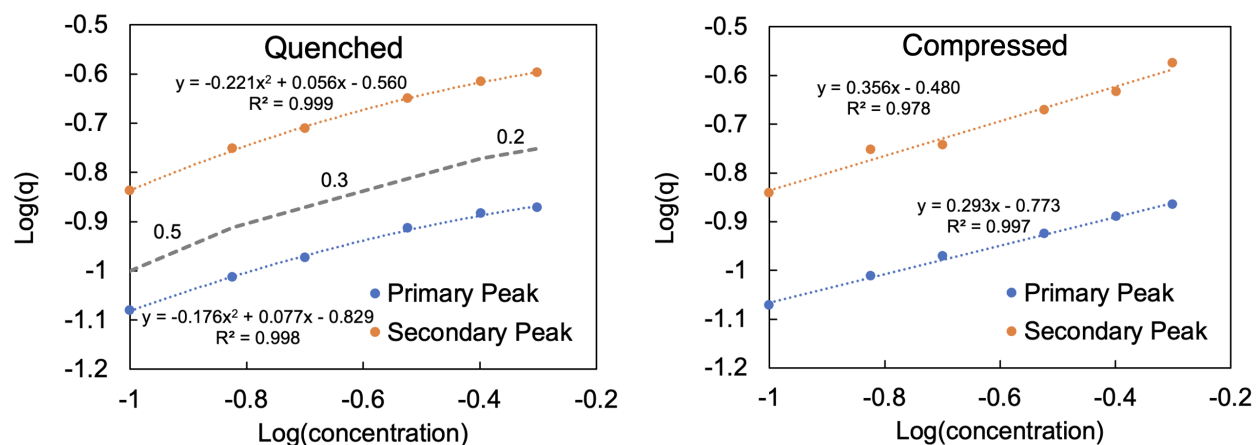


Figure S6: Plot of $\text{Log}(q)$ vs $\text{Log}(\text{concentration})$ for the primary and secondary PE peaks. The quenched data is fit to a quadratic function, the compressed data is fit to a line.

The radial distribution functions (Figure S7) provide a comparison of the local morphological structure as a function of concentration. The quenched and compressed morphologies are very similar. For the 10% w/v poor solvent morphologies, all cross-pair correlations (e.g. 1:4, 1:5, 4:5) decrease together due to counterion condensation, and a large free volume exists

between chains. In contrast, for 50% w/v poor solvent morphologies, the polymer-ion cross-pair correlations (e.g. 1:4, 1:5) show out-of-phase dependence with the self-pair correlations (e.g. 1:1, 4:4, 5:5) indicating that there is a microphase separation of ion-rich regions and polymer rich regions. Interestingly, at 50% w/v, the ion-rich region is dense and confined enough such that there is a positive peak in the counterion (5:5) pair correlation function at 1-3 σ .

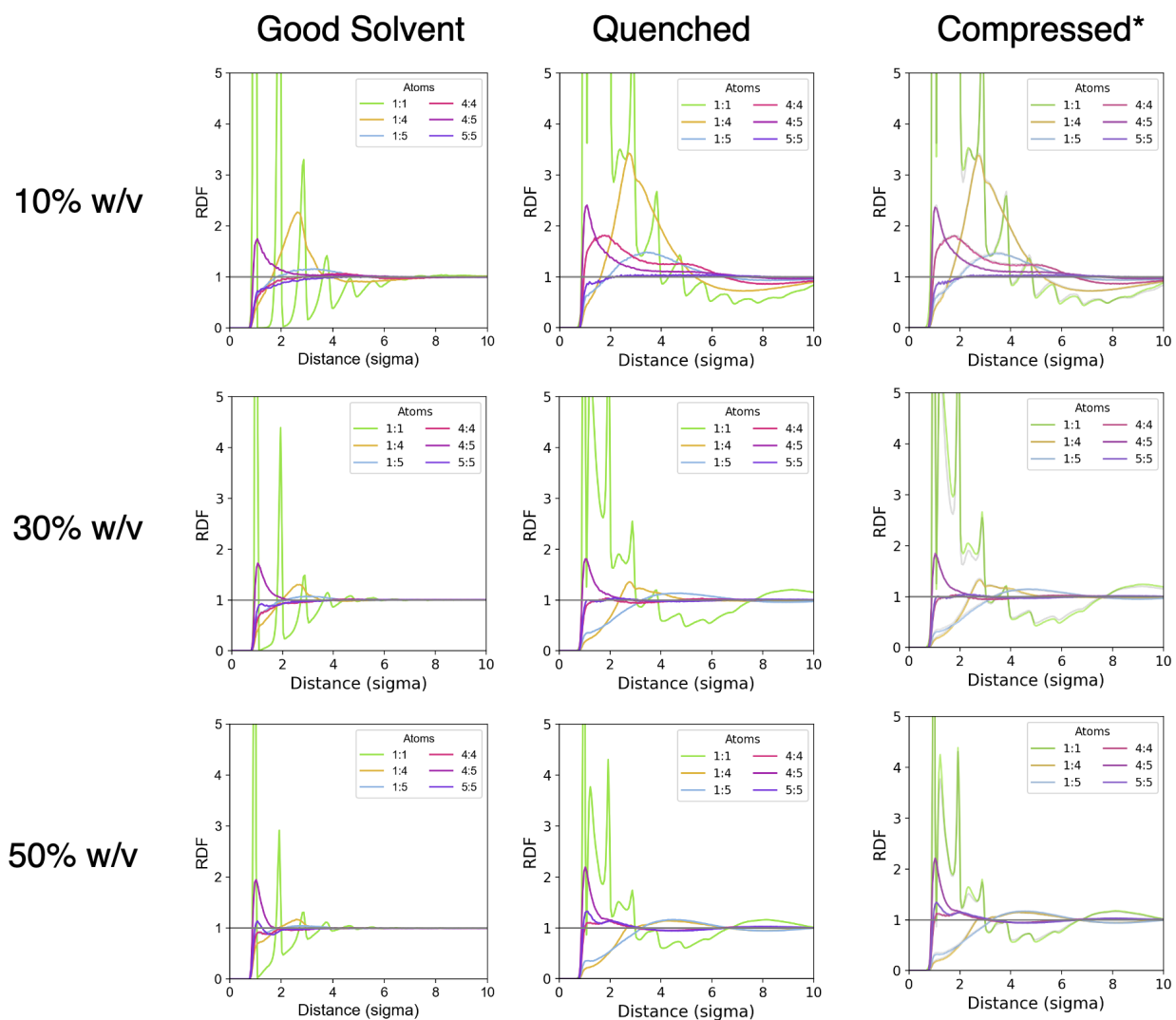


Figure S7: Radial distribution functions of pairs of bead types. Bead types are as follows: 1 - backbone, 4 - pendant cation, 5 - counter-anion. All plots are averages over 51 snapshots. *The quenched data is overlaid in gray on the compressed plot to simplify quantitative comparison.

Bundling Algorithm

Since, to our knowledge, there are no established algorithms for computing spatially heterogeneous estimations of fiber thickness in anisotropically stacking polymer systems, we have devised a bundling algorithm to provide such estimations. At a high level, the bundling algorithm can be described by the following four steps, with each step shown in Figure S1a with colors representing each iteration of the algorithm, starting with red and ending with green. The final results of the algorithm are shown in Figure S1b.

For each monomer in the morphology:

1. Block off the n_{block} neighboring monomers on the current chain (solid colored lines in Figure S1a). This prevents recounting monomers in the same chain as contributing to the fiber thickness.

2. If there are more than n_{size} monomers in the current list of monomers, limit the size of all continuous blocks of monomers on the same chain to n_{size} monomers (black X's in Figure S1a). This step restricts the width of the search for new monomers (step 4), keeping the measured fiber thickness roughly parallel to the direction of π -stacking.

3. For each separate continuous block of monomers in the current list, found in step 2, add one to the calculated fiber thickness.

4. Look for new monomers within r_{cut} of the current list of monomers (semi-transparent ellipses in Figure S1a). New monomers become the current list of monomers in Step 1 (filled ellipses in Figure S1a). If no new monomers are found, exit.

Repeat steps 1-4 until no new monomers are found. In the example, the red monomer in Figure S1a would have a fiber thickness of six because six blocks of monomers are found by the algorithm: one on the first (red) iteration, two on the second (orange) iteration, two on the third (yellow) iteration, and one on the fourth (green) iteration. This process is repeated independently for each individual monomer in the system. The results of this algorithm for several monomers are shown in Figure S1b.

The specific parameter values used in the algorithm above ($n_{block} = 5$, $n_{size} = 3$ monomers,

$r_{cut} = 1.7 \sigma$) were optimized to produce estimates of fiber thickness consistent with a visual examination of the poor-solvent MD trajectories. A more detailed pseudocode is presented below.

```
for monomomer m:
    avail = ones(n, dtype = bool) # monomers available to be added to the fiber
    newnet = zeros(n, dtype = bool) # monomers to be added in the next iteration
    newnet[m] = 1
    fiber = 0 #fiber thickness
    while sum(newnet) != 0:
        js = where(newnet == True)[0] #current monomers are "js"
        # Step 1. Block off n_block = 5 monomers along the chain
        for j in js:
            for monomers in j +/- 5 along the same chain:
                avail[monomers] = 0
        # Step 2. Restrict block size to n_size = 3 monomers
        j = 0
        while j < len(js)-3:
            if js[j+3]-js[j] == 3 and both monomers are on the same chain:
                center = center of the continuous block
                delete js > 1 away from center
        # Step 3. Increase fiber thickness 1 for each block
        fiber += 1
        for j in range(len(js)-1):
            if (js[j+1]-js[j]) > 2:
                fiber += 1
        # Step 4. Find new monomers
        newnet = zeros(n, dtype = bool) #clear new monomers
```

```

for j in js:
    newnet = (A[j] & avail) #A = n x n Adjacency matrix
return(fiber)

```

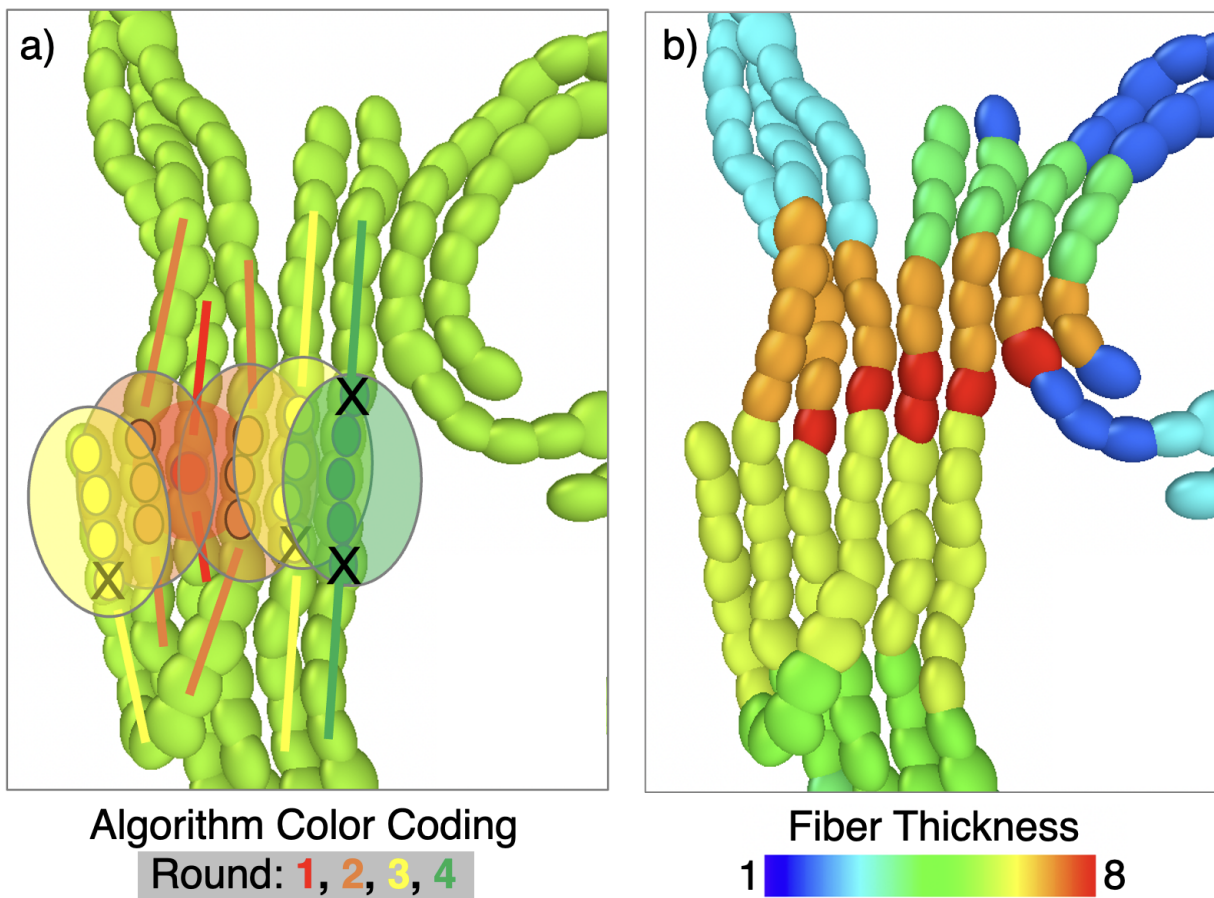


Figure S8: Snapshot of a poor-solvent morphology with a) a demonstration of the bundling algorithm operating on a single monomer (red circle), and b) the final result of the bundling algorithm on all monomers in the snapshot.

Network Structure Characterization

The time dependence of the number and size of the networks is shown in Figure S9. The good solvent simulations (dotted lines) appear equilibrated, as do the poor solvent compressed simulations (dashed lines). The quenched morphology (solid line) appears to be

deaggregating at 10% and 15% w/v. We still chose to analyze the final 100-150 $k\tau$ of these simulations for the sake of consistency, and because we want to analyze a kinetically trapped, highly connected network.

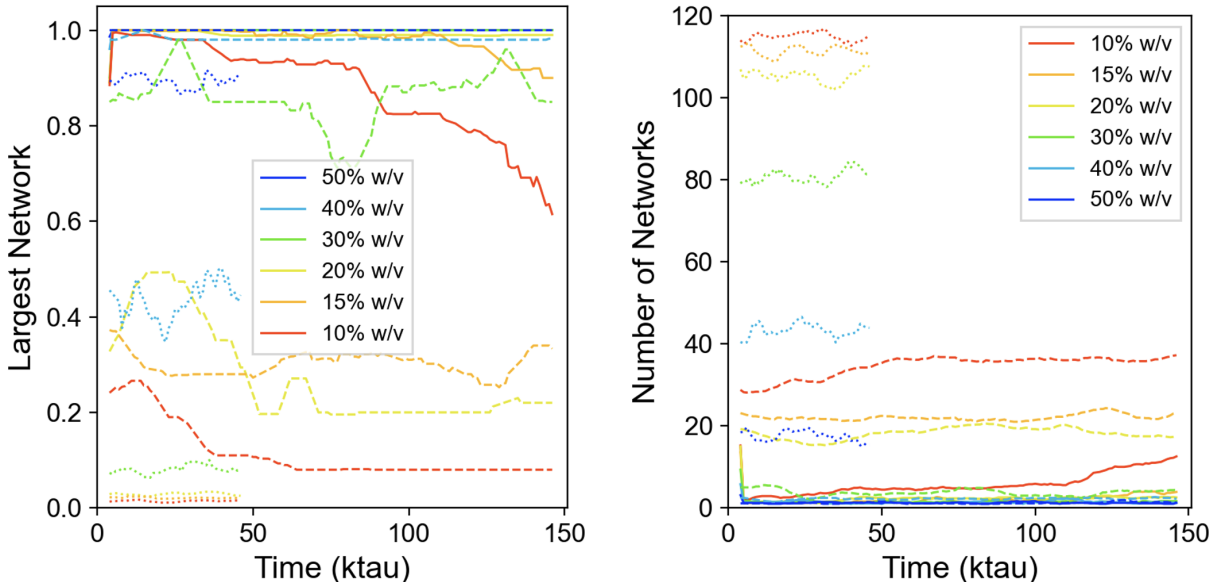


Figure S9: Time dependence of the largest network size (left) and the number of networks (right) for all simulations. Solid lines correspond to quenched simulations; dashed lines correspond to compressed simulations; dotted lines correspond to good solvent simulations. Data was taken every 1 $k\tau$, and the moving average over nine $k\tau$ is plotted.

The network connectivity of the CPE chains is an important descriptor for understanding electronic mobility. Figure S10 shows that the number and sizes of the networks in poor solvent are insensitive to the electronic coupling threshold value over the physical range of threshold values. This indicates that these networks are well connected through π -stacking, and the individual networks are well separated through-space, providing confidence in this metric to describe poor-solvent morphologies. In contrast, the number and sizes of networks in good solvent morphologies are very sensitive to threshold because the inter-chain networks are neither well connected via π -stacking (only coming in contact by fluctuations) nor are they well separated through-space.

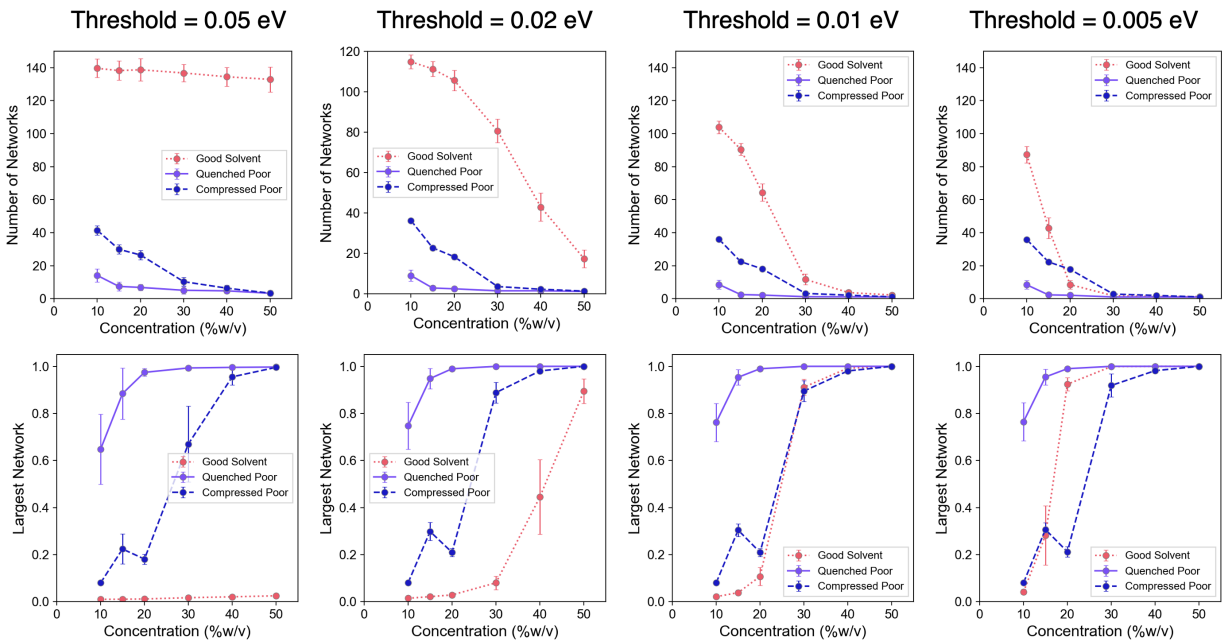


Figure S10: The number of networks (top) and the size of the largest network as a fraction of total monomers in the system (bottom) for several threshold electronic coupling values. The maximum electronic coupling produced by π -stacking in our model is ~ 0.08 eV, so any value above this results in exclusively independent interchain networks.

To further aid in the characterization of the network structure, a UMAP projection of the poor solvent morphologies was generated to visualize how well the poor solvent morphologies are connected. In this case, UMAP was used to take the distances between anisotropic backbone beads (3D with periodic boundaries) and project them down to 2D without periodic boundaries. Note that the UMAP algorithm is stochastic and does not rigorously preserve all connectivity of the higher dimensional object.

The UMAP projections show that at 10% and 20% w/v, the quenched morphology is more connected than the compressed morphology in agreement with the analysis of networks above. However, at 50% w/v, the compressed morphology has regions of thicker fibers connected by stronger bridges, whereas the quenched morphology has a larger number of weaker bridges across its morphology, in agreement with the fiber thickness results (Figure 4). These results help explain why the HOMO IPRs in the compressed morphology are larger than in the quenched morphology, resulting in a higher mobility.

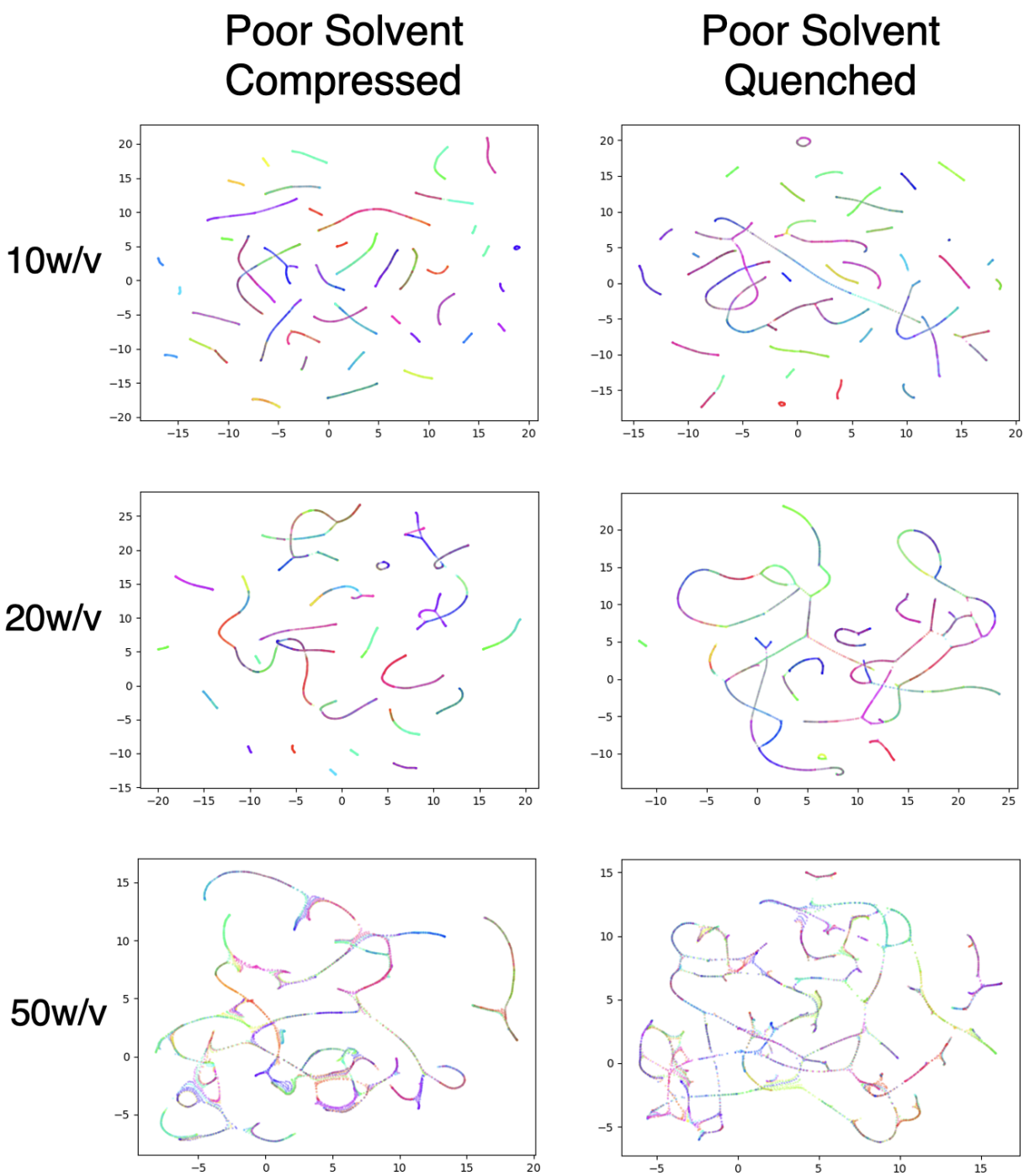


Figure S11: UMAP projection of the quenched and compressed morphologies at 10%, 20%, and 50% w/v. Monomers in the same chain have similar colors and each monomer is semi-transparent to make overlapping chains more apparent.

Electronic Structure Characterization

The ability of ions to alter electronic transport in CPEs is a key feature enabling them to be used as mixed ionic-electronic conductors. Therefore, the electrostatic disorder induced on the backbone of the CPE was calculated to quantify the magnitude of the disorder and its dependence on morphology. Figure S12a shows that there is a net positive electrostatic potential on the backbone beads, consistent with the ability of CPEs pendant ions to enable self-doping. Figure S12b shows that the predicted magnitude of the electrostatic disorder is small ($< 1k_B T$) for all morphologies, and does not significantly impact the electronic properties of the CPEs. For comparison, a Gaussian energetic disorder (associated with disorder not present in the CG model, e.g. solvent polarization) of up to 0.1 eV was added to each monomer but had no qualitative impact on the conclusions.

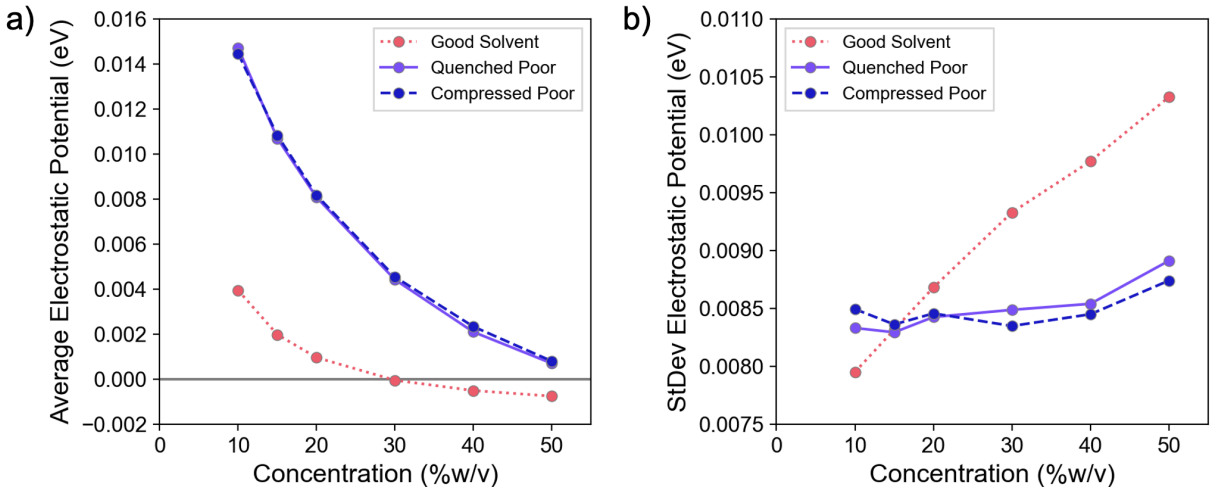


Figure S12: a) Average electrostatic potential energy of anisotropic backbone beads, and b) their standard deviation. The average electrostatic energy is typically positive because the pendant ions are closer to the backbone than the counteranions. This situation is reversed in good solvent at high concentrations as counteranions diffuse closer to the backbone than the pendant cations which are kept at a distance by the side chains. This counterion diffusion in good solvent also increases the standard deviation of the backbone potential energy, whereas in poor solvent the π -stacking reduces how close counter-anions can diffuse towards the backbone (see RDFs, Figure S7).

To aid visualization of how the electrostatic potential varies across a morphology, Figure

S13 shows an example morphology with each backbone bead colored by its electrostatic potential.

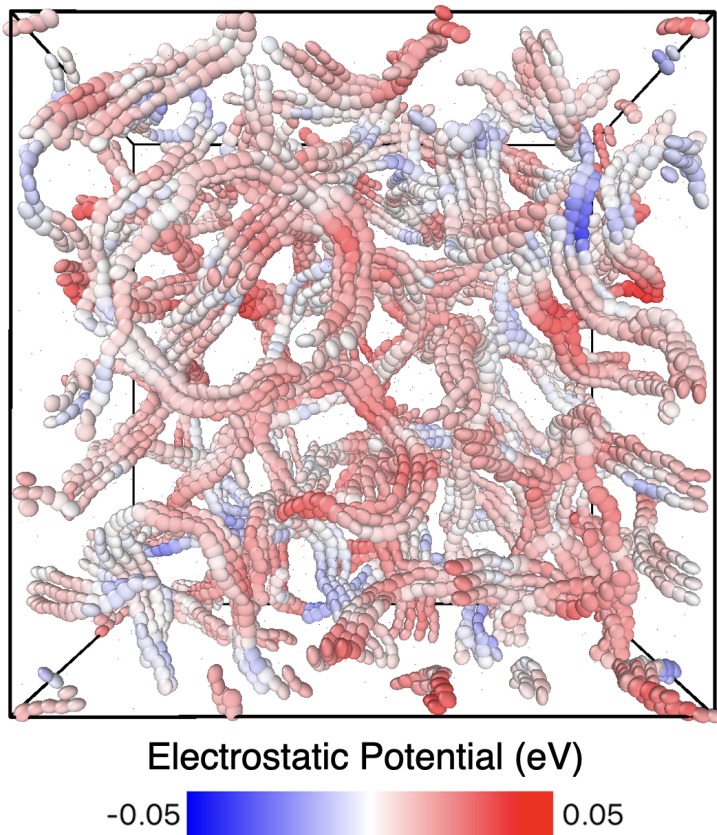


Figure S13: Representative configurational snapshot of the 20% w/v quenched morphology with backbone beads colored by electrostatic potential. Only backbone beads are shown for clarity. The CPE pendant ions are positive, causing the average electrostatic potential on a backbone bead to be positive.

The model presented in this work does not include any onsite energy disorder in the Hamiltonian except for electrostatic induced disorder. Therefore, additional random Gaussian-distributed disorder was added to each monomer to assess the impact of additional onsite disorder on the IPR and final transport properties. The results of this analysis are shown in Figure S14. The addition of 0.1 eV disorder was found to have a moderate impact on mobility, while disorder of 0.3 eV was found to strongly reduce mobility. Figure S17 also shows which pairs of orbitals contribute most to the mobility of a morphology, revealing that long-distance hops (up to half the box length) contribute most to the calculated mobility of

the system, even when additional disorder is added to the morphology.

Quenched 20% w/v				
Disorder (std dev)	0.0 eV	0.1 eV	0.2 eV	0.3 eV
Mobility	6E12	2E12	1.2E11	3E8
Average IPR	40	34	26	20

Compressed 50% w/v				
Disorder (std dev)	0.0 eV	0.1 eV	0.2 eV	0.3 eV
Mobility	1.2E13	1.2E13	4E12	2E11
Average IPR	63	54	39	28

Figure S14: The average mobility and IPR for two morphologies (quenched 20% w/v and compressed 50% w/v) with added amounts of Gaussian onsite disorder. Results are averaged over 50 $k\tau$.

The electronic mobility (Eq 11) depends on the hopping rates and populations of the HOMOs in a morphology, which depend on the overlap between two MOs, their IPR, and the energy difference between those MOs (Eq 5). Figures S15 and S16 show the IPR of the morphologies, revealing that the HOMOs of the more concentrated poor-solvent morphologies are much more delocalized than the good solvent or more dilute morphologies. The DOS of the morphologies also shows that these more delocalized MOs are also more sparsely populated, with the HOMOs tail extending almost 0.2 eV higher than in the good solvent case, increasing the energy gap between orbitals expected to participate in electron transfer. The mobility results indicate that the delocalization of the HOMOs increases the mobility more than the tighter density of states. To further quantify the trends, the average IPR and DOS of the MOs observed to strongly participate in transport (i.e. MOs in the top 0.25 eV of the DOS) are plotted in Figure S16. The fact that the crossover point of the quenched and compressed average IPRs also corresponds to the crossover point of the mobilities indicates that the IPR of the HOMOs plays a significant role in determining electronic transport in CPEs.

It is expected that the calculated mobility for systems containing ten dopants will be larger than that of the mobility from one dopant, as the ten dopant system is able to reach

MOs further from tail of the density of states, which also typically have higher IPRs. This effect is shown in Figure 7 (main text), and the mechanism is supported by the fact that when the leading edge of the density of state is higher in energy, the difference in mobility between one and ten dopants also grows.

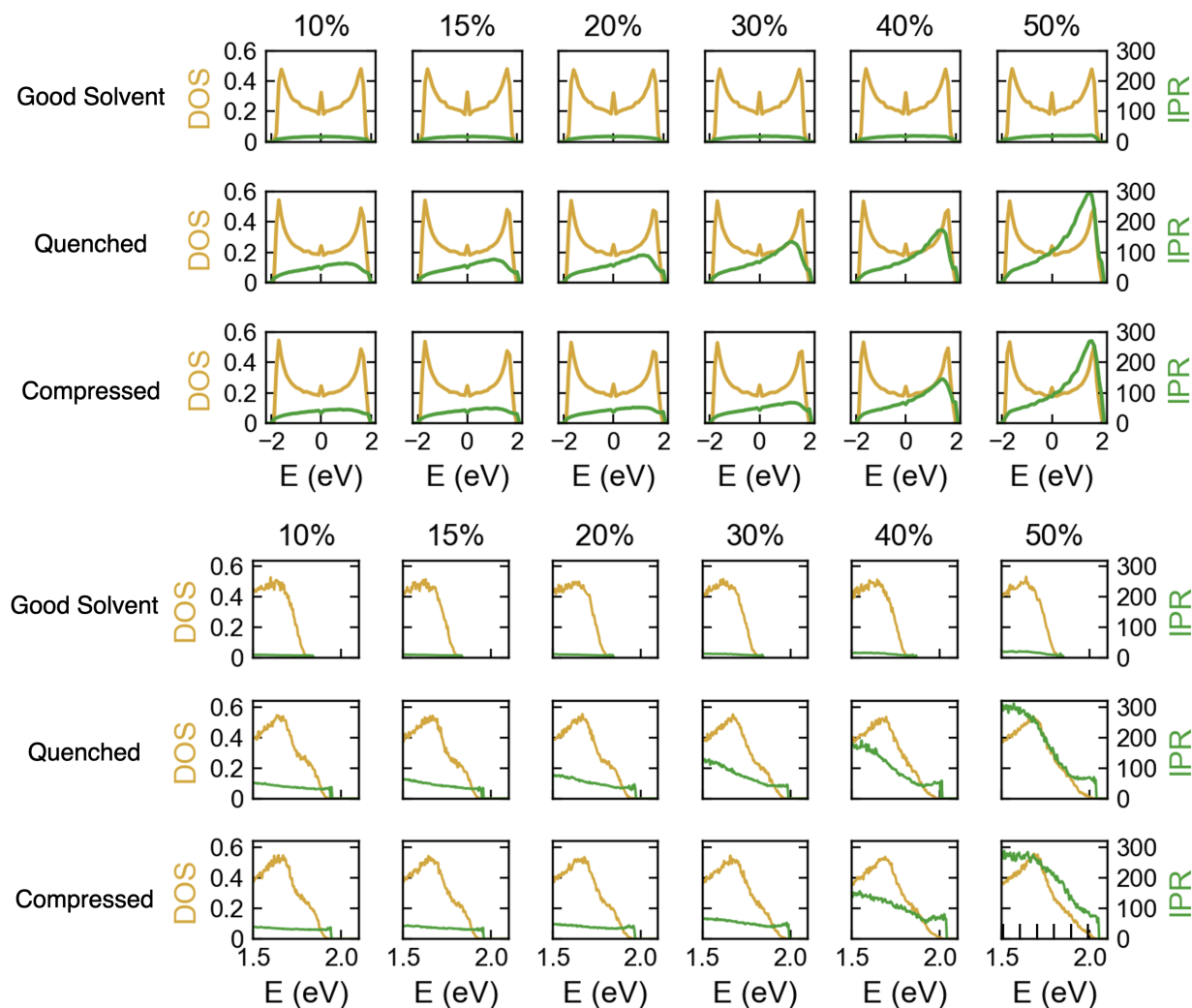


Figure S15: Inverse Participation Ratio (IPR) and density of states (DOS) for each morphology, averaged across 51 snapshots. The upper plots show all 6400 MO (binned every 0.1 eV); the lower plots show only the MOs with energy > 1.5 eV (binned every 0.005 eV, to provide additional clarity about the states contributing to charge transport).

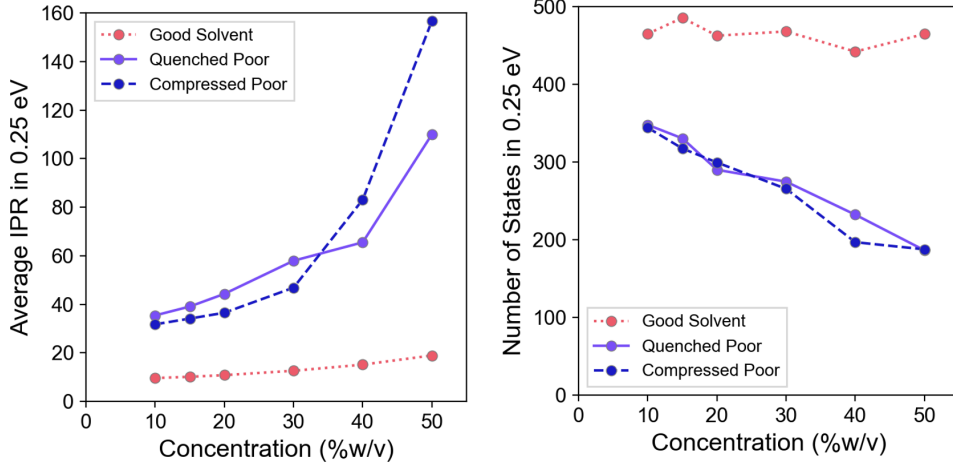


Figure S16: The average IPR (left) and total number of states (right) within 0.25 eV of the HOMO-1 orbital. Results are averaged over the 50 $k\tau$ production run. The HOMO-1 was chosen as a reference point because sometimes the HOMO was separated from the bulk of the DOS, making it an inconsistent reference point.

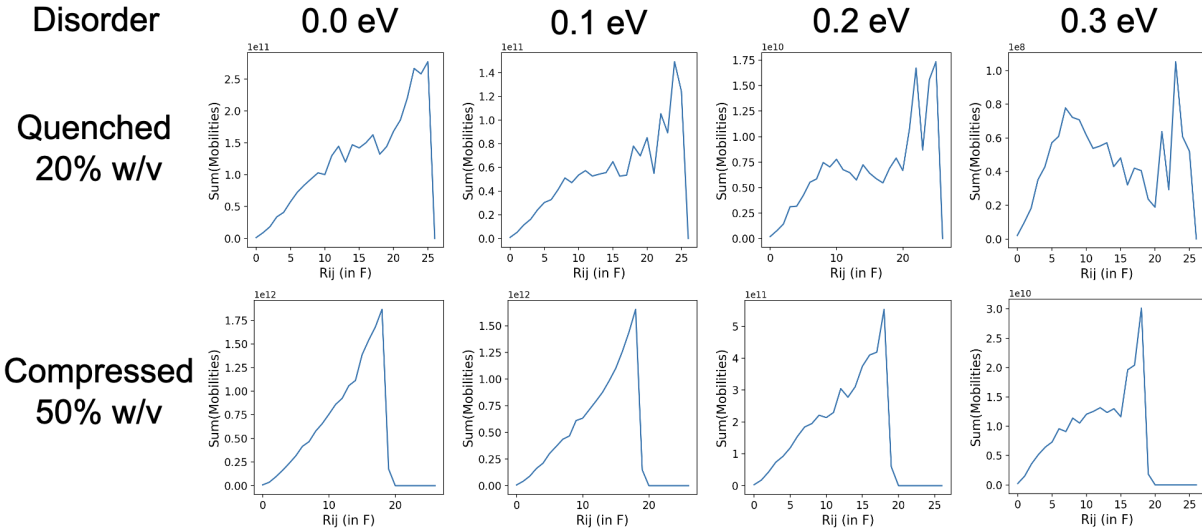


Figure S17: The contributions of hops at various distances (R_{ij}) to the total electronic mobility. The mobility between all pairs of MOs i and j are binned by distance in the direction of the electric field (F) and summed. for each axis in each snapshot, and then averaged across 50 $k\tau$. The column with 0.0 eV of disorder is the same result as presented in the main text. The other disorder values correspond to the same results as Figure S14.

CPE Diffusion

The diffusion constant for the CPE center of mass over the 5-20 k τ timescale is shown in Figure S18. In good solvent, CPE chains are unaggregated and free to move independently of each other on long time scales, making diffusion fast relative to poor solvent CPEs. In low density poor solvent (<20% w/v), CPE diffusion is faster in compressed simulations than quenched simulations, presumably because the chains are less connected and therefore their diffusion is less restricted. At high density (>30% w/v) the trend is reversed, presumably because the compressed chains are more tightly bound (evidenced by their thicker fibers, Figure 4 (main text), and supported by UMAP analysis, Figure S11) causing each chain's motions to be more strongly restricted by the other chains in the fiber.

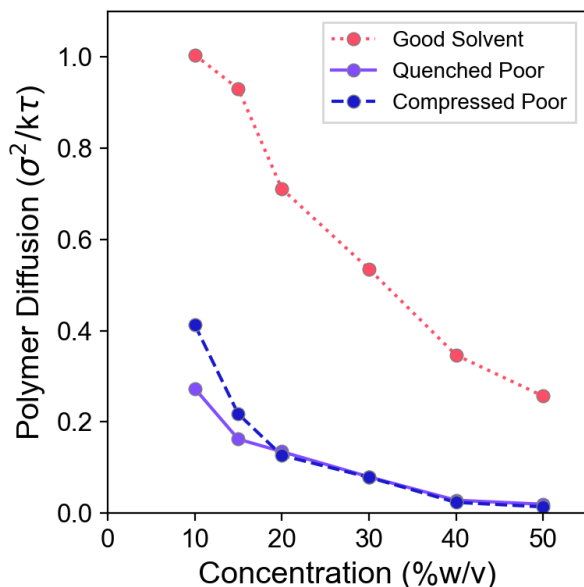


Figure S18: Polymer diffusion constant vs. concentration, as estimated via the mean squared displacement values between 5 - 20 k τ . Diffusion was approximately 2-5 faster at < 5 k τ .

Example MSD vs. Time plots of the ions and polymers are presented in Figure S19.

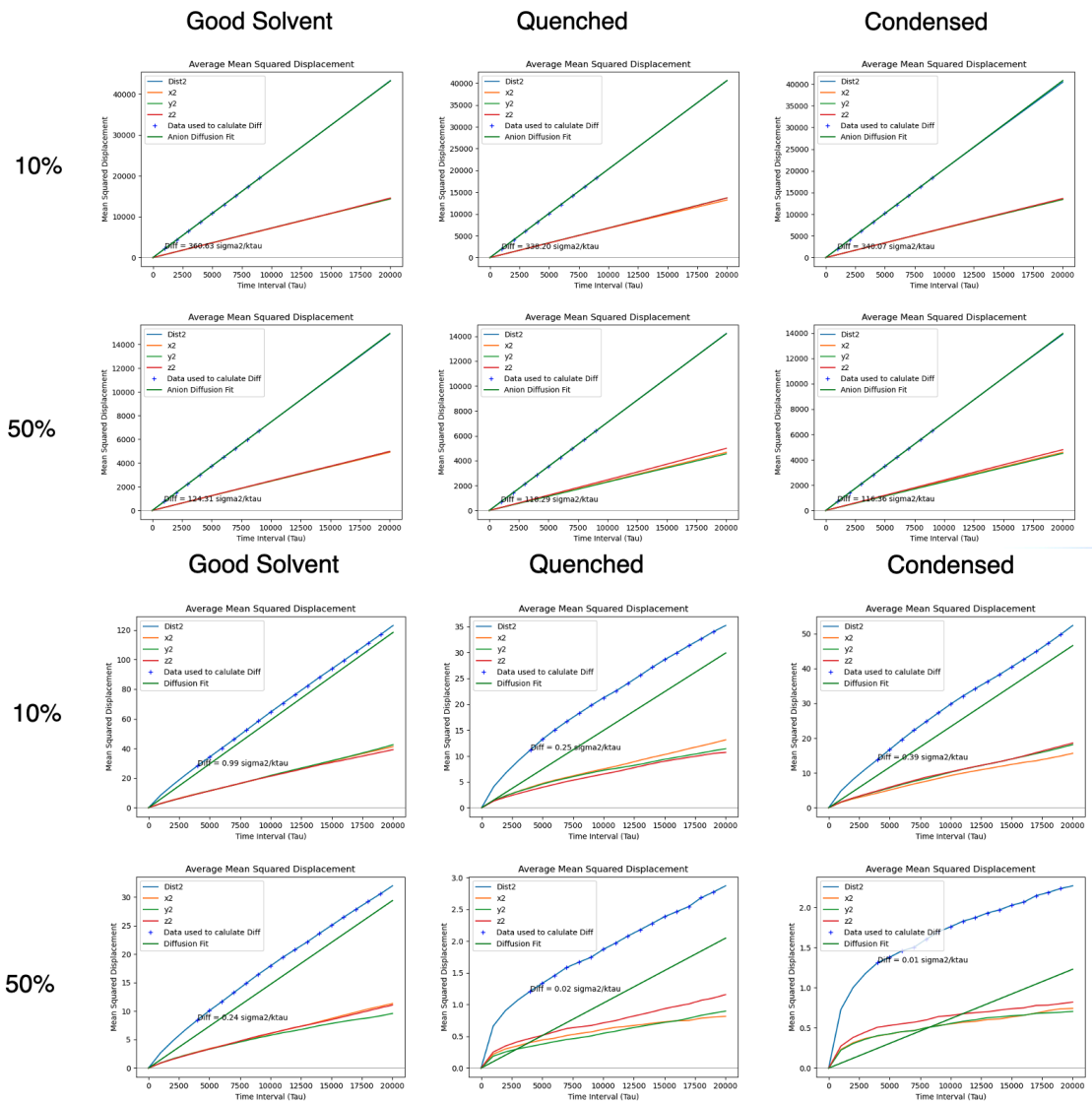


Figure S19: Anion (top) and polymer (bottom) Mean Standard Displacement (MSD) vs. Time. The MSD along the x, y, and z axes are labeled x2, y2, and z2 respectively. The distance MSD is labeled Dist2. The points used to calculate the diffusion constant via a best fit line are labeled with a blue cross. The fitted diffusion constant is annotated on the plot, and a line with the same slope (passing through the origin) is labeled as Diffusion Fit.

While not explicitly presented in the main text, we note that the persistence lengths of CG simulations are in agreement with previous results and physical expectations. The intrinsic persistence lengths of the modeled CPEs is expected to be six σ based on the three-body angle constant between neighboring backbone monomers. As expected, the inter-chain electrostatic repulsion led to the chains being slightly stiffer at 10% w/v (7.5σ), returning

to their intrinsic persistence length when the electrostatic correlation length (the length at which electrostatic interactions are screened) decreased below this length scale. [See Dobrynin, Andrey V., and Michael Rubinstein. “Theory of polyelectrolytes in solutions and at surfaces.” *Progress in Polymer Science* 30.11 (2005): 1049-1118.]